

Mapping AC Susceptibility with Quantum Diamond Microscope

Dasika Shishir,^{*,†} Madhur Parashar,^{*,‡} and Kasturi Saha^{*,†}

[†]*Department of Electrical Engineering, Indian Institute of Technology Bombay, Powai, Mumbai-400076, India.*

[‡]*School of Medical Science and Technology, Indian Institute of Technology Kharagpur, Kharagpur, West Bengal, 721302, India*

E-mail: dshishir@iitb.ac.in; madhurparashar@iitkgp.ac.in; kasturis@ee.iitb.ac.in

Abstract

We present a novel technique for determining the microscale AC susceptibility of magnetic materials. We use magnetic field sensing properties of nitrogen-vacancy (NV^-) centers in diamond to gather quantitative data about the magnetic state of the magnetic material under investigation. In order to achieve the requisite speed in imaging, a lock-in camera is used to perform pixel-by-pixel lock-in detection of NV^- photo-luminescence. In addition, a secondary sensor is employed to isolate the effect of the excitation field from fields arising from magnetic structures on NV^- centers. We demonstrate our experimental technique by measuring the AC susceptibility of soft permalloy micro-magnets at excitation frequencies of up to 20 Hz with a spatial resolution of $1.2\,\mu\text{m}$ and a field of view of $100\,\mu\text{m}$. Our work paves the way for microscopic measurement of AC susceptibilities of magnetic materials relevant to physical, biological, and material sciences.

Introduction

Measurement of AC susceptibility is critical and indispensable in investigating magnetic relaxations and phase transitions in various magnetic materials.^{1,2} In AC susceptibility measurements, a small external perturbation of frequency ranging from a few hertz to several tens of kilohertz is applied to observe the dynamic change in the magnetic moment. The magnetic system's relaxation time under investigation, τ , dictates the system's frequency response. Hence, AC susceptibility measurements lead to the characterization of relaxation times. AC susceptibility measurements have been performed in the context of high critical temperature superconductors,^{3,4} spin-glasses, paramagnetic salts,^{5,6} magnetic nano-particles,⁷⁻⁹ and conventional and low-dimensional ferromagnets.^{10,11} In conventional AC susceptometry, the sample under study is excited using a primary coil. The in-phase and quadrature-phase change in magnetization is detected through a secondary coil using a lock-in amplifier.¹² The quadrature-phase signal obtained is proportional to the real part of the susceptibility χ' , and the in-phase signal is proportional to the imaginary part of the susceptibility χ'' . In general, any magnetometer can be turned into a susceptometer if the frequency response of the magnetometer is adequate to measure the change in magnetization at the desired excitation frequencies. As such, SQUID magnetometers,^{13,14} MOKE magnetometers,^{15,16} and electron, neutron, and X-Ray based methods have^{17,18} been utilized to measure AC susceptibility. However, some of these techniques do not give information on the local microscale variations in susceptibility, which might be of great value in many cases, say near the vortices in a high-Tc superconductor. Some of the methods described above, though they have good spatial resolution down to 10 nm, fail to provide quantitative information on magnetic properties like dipole moment and susceptibility.

In this letter, we present a spatially resolved dynamic AC susceptibility experimental approach and illustrate it by measuring the AC susceptibility of a collection of microfabricated permalloy ($\text{Ni}_{0.8}\text{Fe}_{0.2}$) micromagnets. This work builds upon the recent demonstrations of high-speed wide-field magnetic imaging using a per-pixel lock-in amplifier camera^{19,20} in

a quantum diamond microscope.²¹ A lock-in camera significantly enhances the per-pixel sensitivity due to the rejection of noise outside the modulation frequency bandwidth. Additionally, a lock-in camera utilizes the full-well capacity of a CMOS sensor more efficiently to enhance the dynamic range of the collected fluorescence.^{19,22} To perform dynamic magnetic imaging, a single microwave frequency is chosen in the spectrum of negatively charged nitrogen-vacancy (NV^-) centers, where the photoluminescence (PL) varies linearly with the change in external magnetic field.^{23,24} The linear range is limited to the linewidth of the spectrum, which is typically 1 MHz to 2 MHz. This frequency shift corresponds to a change in the magnetic field of 10 μT to 20 μT . However, the AC excitation field is varied by a few milli-Teslas² to perform AC susceptibility measurements. This variation falls outside the dynamic range of lockin-camera-based quantum diamond microscope, limiting its use in dynamic imaging of magnetic materials. To mitigate the problem mentioned above, we use a secondary sensor to dynamically set the microwave frequency such that NV^- PL response falls in a regime that is always linear to the changes in small magnetic fields arising from the magnetic material under study. Using a second sensor effectively decouples the excitation field from the fields arising from the magnetic materials as a response to the excitation field. With this technique, a variety of excitation fields may be used to investigate different materials with reasonable SNR. For instance, a magnetic material with low susceptibility that needs a strong excitation to cause a change in magnetic moment can also be detected. Using our technique, we detect a change in the magnetic moment of 36 fJ T⁻¹ by applying an AC field of 1 mT of up-to 20 Hz while maintaining a spatial resolution of 1.2 μm .

Results and Discussion

The experimental platform is based on optically detected magnetic resonance (ODMR)²⁵ signal from NV^- centers in diamond is shown in Fig. 1 (a). We place an array of circular Permalloy (Py) micromagnets of 5 μm diameter and 30 nm thickness separated by 25 μm from

center to center fabricated on a silicon substrate on top of a diamond chip. The diamond chip is $4 \times 4 \text{ mm}^2$ electronic grade, 99.99% ^{12}C diamond from Element 6, with approximately $1 \mu\text{m}$ thick ^{15}N doping. The concentration of NV^- in this layer is around 1-2 ppm. The diamond crystal has $\{100\}$ front facet and $\langle 110 \rangle$ edge orientation. A 532 nm, 0.5 W laser is incident on the diamond layer through a $100\times$ air objective of numerical aperture 0.9. The overall magnification of the system is $34\times$. Each camera pixel is $40 \mu\text{m}$. Hence, each pixel captures PL from $1.17 \mu\text{m} \times 1.17 \mu\text{m}$ area of the diamond. The NV^- center emits a red PL when excited with the 532 nm laser. The PL is collected through the same objective and focused on a wide-field lock-in camera (Heliotis Helicam C3) after passing through necessary filters to reject the green excitation at 532 nm. The NV^- center is a spin-1 system with a bright $m_S = 0$ state and relatively dark $m_S = \pm 1$ states. In the absence of a magnetic field, $m_S = \pm 1$ states are nearly degenerate, and are separated from $m_S = 0$ by a zero-field splitting of 2.87 GHz. In the presence of a magnetic field, the degeneracy between $m_S = \pm 1$ is lifted, given as ²⁵

$$\nu_{\pm} = D \pm \gamma_e B_{NV}, \quad (1)$$

where ν_{\pm} are resonance frequencies corresponding to $m_S = 0 \rightarrow \pm 1$ transition, D is the zero-field splitting 2.87 GHz, γ_e is the electron gyro-magnetic ratio equal to 28 MHz mT^{-1} , and B_{NV} is the magnetic field along one of the four possible diamond crystallographic orientations. When the frequency of an externally applied microwave signal is close to one of the eight possible resonant frequencies, there is a drop in PL. An external magnetic field is applied using a current carrying coil of 100 turns and 7 cm diameter. At the same time, a signal generator sweeps the microwave signal via a loop antenna on which the diamond is placed. The microwave signal is amplitude modulated at 8 kHz using a microwave switch, and the resultant modulations in the PL are demodulated at a pixel level by the lock-in-camera. A more detailed account of the experimental setup and the operation of lock-in-camera in this context is provided in Ref. ¹⁹

First, we perform DC characterization of the micro-magnets. To do so, we obtain the

full ODMR spectrum at each value of the applied external field as shown in Fig. 1(b). The externally applied magnetic field not only affects the NV^- centers in diamond but also affects the magnetic state of micro-magnets. In Fig. 2, we show the effect of an external magnetic field on the state of micro-magnets. In Fig. 2(a), the stray magnetic field arising from the the micro-magnetic array is shown. The total applied magnetic field is 3.34 mT, with an in-plane component of 2.59 mT. The applied vector magnetic fields are obtained by measuring the resonance frequencies of all the four possible NV^- axis and fitting with NV^- spin Hamiltonian.²⁶ Because the shape anisotropy restricts the dipole moment of the micro-magnet to be in-plane,²⁷ we only consider the applied in-plane magnetic field in susceptibility calculations. The stray magnetic field is obtained by extracting the resonant frequency from each pixel by fitting the ODMR response to a function that is a sum of two Lorentzian functions. After the resonant frequency at each pixel is obtained, the median resonance frequency is subtracted from all the pixels. The resultant shifts in resonant frequencies are converted to a magnetic field map by dividing the resonant shifts with electron gyro-magnetic ratio as in Eq. (1). Finally, using the procedure outlined in Ref.,^{28,29} and Supplemental Information (Section 3), the obtained field, which is the field along a NV^- axis is converted into a field along the z axis (pointing out of the diamond plane). In Fig. 2(b), the stray magnetic field from a single micro-magnet at three different externally applied magnetic fields - 0.59 mT, 1.5 mT, and 2.59 mT are shown. Owing to the soft ferromagnetic nature of Py, we observe that the micro-magnets have very low retentivity. This is ascertained by plotting the dipole moment of the micro-magnets as we vary the external magnetic field as shown in Fig. 2(c). The dipole moment is obtained by fitting the magnetic field arising from a cylindrical magnet (See Supplemental Information, Section 2). Using the fit, we estimate the stand-off distance between the NV^- layer and the micro-magnet layer to be around $11.51 \pm 0.08 \mu\text{m}$. The dipole moment increases, nearly linearly with externally applied field with a slope of 36 fJ/ T/mT, 28.1 fJ/ T/mT, and 33.1 fJ/ T/mT for micromagnets A , B , C as labeled in Fig. 2(a). Although, we did not perform measurements on micro-magnets at

zero-field, by extrapolation, we assume that the dipole moment of micro-magnets at zero field is very low (-3.35 fJ T^{-1} , 0.5 fJ T^{-1} , -5.76 fJ T^{-1} for micromagnets A , B , C) respectively. With a volume of $0.59 \mu\text{m}^3$, the volume normalized susceptibility of three micro-magnets labeled A , B , and C were found to be 69.7, 54.4, 64.1 respectively.

We next present the results of dynamic measurements on micro-magnets. The AC susceptibility is measured by applying an excitation ΔH at frequency f_{ac} and measuring the change in the dipole moment Δm of the material under study. The AC susceptibility χ_{ac} is defined as

$$\chi_{ac} = \frac{1}{V} \frac{\Delta m}{\Delta H}, \quad (2)$$

where V is the volume of the micro-magnet. The dynamic measurements are done by applying a single microwave frequency, at a frequency of maximum slope away from the resonance to the microwave antenna and measuring PL response from the diamond. The slope of a Lorentzian at this frequency point is equal to $A/0.77\Gamma$,³⁰ where A is the amplitude of the Lorentzian curve and Γ is the full-width at half-maximum of the Lorentzian curve. Small shifts in resonance from pixel to pixel due to small changes in stray magnetic fields ΔB_{NV} manifest as changes in PL intensity ΔPL as

$$\Delta\text{PL} = \frac{A}{0.77\Gamma} \times \gamma_e \Delta B_{NV}. \quad (3)$$

This makes it possible to reconstruct the magnetic field by recording the PL at a single microwave frequency. However, this method poses a challenge while measuring the dynamic response of magnetic materials to changes in applied magnetic fields. Due to significant shifts in resonance frequency owing to large changes in the applied magnetic field, the PL response is no longer linear to changes in the magnetic field. Hence, Eq. (3) is no longer valid. To overcome this problem, we attach a current sensor of 1.2 kHz bandwidth to the current carrying coil (See Supplemental Information Section 1). The magnetic field from the current carrying coil is always proportional to the current, and the resonance frequency of

the NV^- center is a linear function of the magnetic field. Hence, the resonance frequency of the NV^- center is a linear function of the current in the coil. The output voltage of the current sensor is connected to the signal generator (SRS - SG380), which functions in a voltage-controlled oscillator mode. The output frequency of the function generator is given by

$$f_o = f_c + v \times f_{dev}, \quad (4)$$

where f_o is the output frequency, f_c is the center frequency, f_{dev} is frequency deviation and v is the applied voltage. The center frequency f_c , and the frequency deviation f_{dev} can be set through software. Hence, by carefully choosing the values of f_c , and f_{dev} , one can always ensure that the applied micro-wave frequency is set to a point where the slope and hence the sensitivity is maximum. This kind of a closed loop control ensures that the change in PL, ΔPL given in Eq. (3) always arises from the response of magnetic material under investigation and not the excitation field itself. To perform AC susceptibility measurements we chose two currents in the current carrying coil - 1.45 A, and 3.6 A, which correspond to an in-plane magnetic fields of 0.75 mT and 1.85 mT and a total magnetic field of 0.97 mT and 2.40 mT. The DC stray field images at both of these magnetic fields is shown in Fig. 3(a). We then oscillate the magnetic field at a rate of 0.5 Hz between these two values of magnetic fields and measure the PL at a rate of 1 fps. Each frame is obtained by averaging the PL for 1 s. First few frames are obtained at the lower magnetic field 0.85 mT for reference. The acquisition of camera frames is synchronized with the applied magnetic field. Therefore, alternate frames contain PL maps obtained for lower value of magnetic field and higher value of magnetic field respectively. Alternate frames are then subtracted from each other and scaled according to Eq. (3). Note that the amplitude A and line-width Γ given in Eq. (3) is not uniform throughout the imaging window, and hence the scaling has to be done pixel by pixel. In Fig. 3(a), magnetic field images are shown frame by frame after subtracting the reference frame REF while the magnetic field is low. The subtracted frames are indicative of the change in stray magnetic field produced by the micro-magnets due to the change in

dipole moment. The change in stray magnetic field is directly proportional to the change in dipole moment Δm of Eq.(2). According to the cylindrical model, the change in stray field corresponds to a change of 39.6 fJ T^{-1} in dipole moment. The maximum change in stray field produced by the micro-magnets is $2.9 \pm 0.2 \mu\text{T}$, while in other pixels it is less than that. Note that the sensitivity is for magnetic fields along the direction of NV^- axis, while it will be less for fields that are not along the NV^- axis. Given our mean per pixel sensitivity of $0.9 \mu\text{T}/\sqrt{\text{Hz}}$,¹⁹ we still have to average more cycles to get decent SNR. The volume normalized susceptibility is found to be approximately same as the DC susceptibility $\chi_{ac,0.5} = 73.1, 61, 66.5$ for micromagnets A, B, C . In Fig. 4, we show the results for higher frequencies. At higher frequencies, it is also important to measure the imaginary part of AC susceptibility χ''_{ac} . To facilitate the measurement of χ''_{ac} , we acquire several frames at the lower magnetic field before applying the AC excitation as shown in Fig. 3(b) (labeled as REF). After application of AC excitation, the imaginary part of AC susceptibility is proportional to REF-OFF, $\chi'' \propto \text{REF-OFF}$, and the real part is proportional to ON-OFF, $\chi' \propto \text{ON-OFF}$. In Fig. 4(a), the difference in stray magnetic field ON-OFF and in Fig. 4(b) OFF-REF is shown at a rate 18 Hz for the entire array. At this frequency, we observe no out of phase component in dipole moment as is expected from Py.³¹ Finally in Fig. 4(c), the AC susceptibility at various frequencies for micro-magnets A, B, C are shown. The AC susceptibility for all the frequencies measured are nearly equal to DC susceptibility - $\chi_A = 73 \pm 5$, $\chi_B = 62 \pm 4$, $\chi_C = 67 \pm 4$. The maximum frequency of 18 Hz that we applied in our case was limited by software synchronization pulse that we applied, to synchronize the AC magnetic field and camera acquisition, and the frequency sweep limit of our signal generator, which is 120 Hz. However, without these limitations in place, the higher frequency limit is dictated by the NV^- response time. The fastest response time reported has been around 50 kHz.³² Assuming that at-least 4 demodulation cycles are required for decent SNR, the maximum frequency at which one can operate will be around 10 kHz to 15 kHz.

Conclusion

In conclusion, we propose and demonstrate a method to perform microscopic AC susceptibility measurements using a quantum diamond microscope. We utilized a fast lock-in camera and a secondary sensor to dynamically vary the microwave frequency to measure AC susceptibilities of soft Py micro-magnets. Our work offers quantitative AC characterization over a wide-field of view in contrast to existing state of art spatially resolved AC susceptibility measurement techniques.¹⁷ In particular our work can extend the application of quantum diamond microscope to simultaneously provide quantitative information of magnetic properties as well as relaxation times of biologically relevant individual and agglomerates of magnetic nano-particles.³³⁻³⁵ Overall, our study is significant to physical, biological, and materials sciences and can be used in quantitative dynamic microscopic analyses of magnetic materials.

Author Contribution

D.S., M.P. and K.S. conceived the idea. DS fabricated and characterized the devices, performed all experiments and analysed the data. MP and KS built the initial experimental setup. DS wrote the manuscript in discussion with all authors. KS supervised all aspects of the work.

Acknowledgement

K.S. acknowledges financial support from DST Inspire Faculty Fellowship DST/INSPIRE/04/2016/002284, SERB EMR grant Number EMR/2016/007420, Asian Office of Aerospace Research and Development (AOARD) R&D Grant no. FA2386-19-1-4042 and DST Quest Grant DST/ICPS/QuST/Theme-2/2019/Q-58. K.S. acknowledges the support and usage of fabrication facilities in the IIT Bombay Nano-fabrication facility via the NNetra project sponsored by Department of Science and Technology (DST) and Ministry of

Electronics and Information Technology (MEITY), India. The authors acknowledge insightful discussions with Prof. Anjan Barman (S. N. Bose National Center for Basic Sciences). K.S. also acknowledges useful discussions with Dr. Shamashis Sengupta (CNRS, Université Paris-Saclay) and Prof. Sumiran Pujari (IIT Bombay).

References

- (1) Topping, C. V.; Blundell, S. J. A.C. susceptibility as a probe of low-frequency magnetic dynamics. *Journal of Physics: Condensed Matter* **2018**, *31*, 013001.
- (2) Balanda, M. AC susceptibility studies of phase transitions and magnetic relaxation: Conventional, molecular and low-dimensional magnets. *Acta Phys. Pol. A* **2013**, *124*, 964–976.
- (3) Ishida, T.; Goldfarb, R. B. Fundamental and harmonic susceptibilities of $\text{YBa}_2\text{Cu}_3\text{O}_{7-\delta}$. *Phys. Rev. B* **1990**, *41*, 8937–8948.
- (4) Očko, M.; Živkovic, I.; Prester, M.; Drobac, D.; Ariosa, D.; Berger, H.; Pavuna, D. Consistent behaviour of AC susceptibility and transport properties in magnetic superconductor $\text{RuSr}_2\text{GdCu}_2\text{O}_8$. *Journal of Magnetism and Magnetic Materials* **2004**, *269*, 231–237.
- (5) Ma, Z. et al. Spin-Glass Ground State in a Triangular-Lattice Compound YbZnGaO_4 . *Phys. Rev. Lett.* **2018**, *120*, 087201.
- (6) Bag, P.; Baral, P. R.; Nath, R. Cluster spin-glass behavior and memory effect in $\text{Cr}_{0.5}\text{Fe}_{0.5}\text{Ga}$. *Phys. Rev. B* **2018**, *98*, 144436.
- (7) Zhong, J.; Lucht, N.; Hankiewicz, B.; Schilling, M.; Ludwig, F. Magnetic field orientation dependent dynamic susceptibility and Brownian relaxation time of magnetic nanoparticles. *Applied Physics Letters* **2019**, *115*, 133102.

- (8) Zhong, J.; Schilling, M.; Ludwig, F. Magnetic nanoparticle thermometry independent of Brownian relaxation. *Journal of Physics D: Applied Physics* **2017**, *51*, 015001.
- (9) Wu, K.; Liu, J.; Su, D.; Saha, R.; Wang, J.-P. Magnetic Nanoparticle Relaxation Dynamics-Based Magnetic Particle Spectroscopy for Rapid and Wash-Free Molecular Sensing. *ACS Applied Materials & Interfaces* **2019**, *11*, 22979–22986.
- (10) Bauer, A.; Neubauer, A.; Franz, C.; Münzer, W.; Garst, M.; Pfeleiderer, C. Quantum phase transitions in single-crystal $\text{Mn}_{1-x}\text{Fe}_x\text{Si}$ and $\text{Mn}_{1-x}\text{Co}_x\text{Si}$: Crystal growth, magnetization, ac susceptibility, and specific heat. *Phys. Rev. B* **2010**, *82*, 064404.
- (11) Zhang, X.-Y.; Wang, Y.-X.; Tartaglia, T. A.; Ding, T.; Gray, M. J.; Burch, K. S.; Tafti, F.; Zhou, B. B. ac Susceptometry of 2D van der Waals Magnets Enabled by the Coherent Control of Quantum Sensors. *PRX Quantum* **2021**, *2*, 030352.
- (12) Laurent, P.; Fagnard, J. F.; Vanderheyden, B.; Babu, N. H.; Cardwell, D. A.; Ausloos, M.; Vanderbemden, P. An ac susceptometer for the characterization of large, bulk superconducting samples. *Measurement Science and Technology* **2008**, *19*, 085705.
- (13) Hibbs, A. D.; Sager, R. E.; Kumar, S.; McArthur, J. E.; Singaas, A. L.; Jensen, K. G.; Steindorf, M. A.; Aukerman, T. A.; Schneider, H. M. A SQUID-based ac susceptometer. *Review of Scientific Instruments* **1994**, *65*, 2644–2652.
- (14) Buchner, M.; Höfler, K.; Henne, B.; Ney, V.; Ney, A. Tutorial: Basic principles, limits of detection, and pitfalls of highly sensitive SQUID magnetometry for nanomagnetism and spintronics. *Journal of Applied Physics* **2018**, *124*, 161101.
- (15) Pohlit, M.; Muscas, G.; Chioar, I.-A.; Stopfel, H.; Ciuciulkaite, A.; Östman, E.; Pappas, S. D.; Stein, A.; Hjörvarsson, B.; Jönsson, P. E.; Kapaklis, V. Collective magnetic dynamics in artificial spin ice probed by ac susceptibility. *Phys. Rev. B* **2020**, *101*, 134404.

- (16) Arnold, C. S.; Dunlavy, M.; Venus, D. Magnetic susceptibility measurements of ultra-thin films using the surface magneto-optic Kerr effect: Optimization of the signal-to-noise ratio. *Review of Scientific Instruments* **1997**, *68*, 4212–4216.
- (17) Römer, F. M.; Kronast, F.; Heyne, L.; Hassel, C.; Banholzer, A.; Kläui, M.; Meckenstock, R.; Lindner, J.; Farle, M. Spatially resolved measurements of the ferromagnetic phase transition by ac-susceptibility investigations with x-ray photoelectron emission microscope. *Applied Physics Letters* **2010**, *96*, 122501.
- (18) Aspelmeier, A.; Tischer, M.; Farle, M.; Russo, M.; Baberschke, K.; Arvanitis, D. Ac susceptibility measurements of magnetic monolayers: MCXD, MOKE, and mutual inductance. *Journal of Magnetism and Magnetic Materials* **1995**, *146*, 256–266.
- (19) Parashar, M.; Bathla, A.; Shishir, D.; Gokhale, A.; Bandyopadhyay, S.; Saha, K. Sub-second temporal magnetic field microscopy using quantum defects in diamond. *Scientific Reports* **2022**, *12*, 8743.
- (20) Webb, J. L.; Troise, L.; Hansen, N. W.; Frellsen, L. F.; Osterkamp, C.; Jelezko, F.; Jankuhn, S.; Meijer, J.; Berg-Sørensen, K.; Perrier, J.-F. m. c.; Huck, A.; Andersen, U. L. High-Speed Wide-Field Imaging of Microcircuitry Using Nitrogen Vacancies in Diamond. *Phys. Rev. Applied* **2022**, *17*, 064051.
- (21) Scholten, S. C.; Healey, A. J.; Robertson, I. O.; Abrahams, G. J.; Broadway, D. A.; Tetienne, J.-P. Widefield quantum microscopy with nitrogen-vacancy centers in diamond: Strengths, limitations, and prospects. *Journal of Applied Physics* **2021**, *130*, 150902.
- (22) Wojciechowski, A. M.; Karadas, M.; Huck, A.; Osterkamp, C.; Jankuhn, S.; Meijer, J.; Jelezko, F.; Andersen, U. L. Contributed Review: Camera-limits for wide-field magnetic resonance imaging with a nitrogen-vacancy spin sensor. *Review of Scientific Instruments* **2018**, *89*, 031501.

- (23) Barry, J. F.; Turner, M. J.; Schloss, J. M.; Glenn, D. R.; Song, Y.; Lukin, M. D.; Park, H.; Walsworth, R. L. Optical magnetic detection of single-neuron action potentials using quantum defects in diamond. *Proceedings of the National Academy of Sciences* **2016**, *113*, 14133–14138.
- (24) Clevenson, H.; Trusheim, M. E.; Teale, C.; Schröder, T.; Braje, D.; Englund, D. Broad-band magnetometry and temperature sensing with a light-trapping diamond waveguide. *Nature Physics* **2015**, *11*, 393–397.
- (25) Rondin, L.; Tetienne, J.-P.; Hingant, T.; Roch, J.-F.; Maletinsky, P.; Jacques, V. Magnetometry with nitrogen-vacancy defects in diamond. *Reports on Progress in Physics* **2014**, *77*, 056503.
- (26) Schloss, J. M.; Barry, J. F.; Turner, M. J.; Walsworth, R. L. Simultaneous Broadband Vector Magnetometry Using Solid-State Spins. *Phys. Rev. Applied* **2018**, *10*, 034044.
- (27) Roy, K.; Bandyopadhyay, S.; Atulasimha, J. Switching dynamics of a magnetostrictive single-domain nanomagnet subjected to stress. *Phys. Rev. B* **2011**, *83*, 224412.
- (28) Kehayias, P.; Bussmann, E.; Lu, T.-M.; Mounce, A. M. A physically unclonable function using NV diamond magnetometry and micromagnet arrays. *Journal of Applied Physics* **2020**, *127*, 203904.
- (29) Lima, E. A.; Weiss, B. P. Obtaining vector magnetic field maps from single-component measurements of geological samples. *Journal of Geophysical Research: Solid Earth* **2009**, *114*.
- (30) Dréau, A.; Lesik, M.; Rondin, L.; Spinicelli, P.; Arcizet, O.; Roch, J.-F.; Jacques, V. Avoiding power broadening in optically detected magnetic resonance of single NV defects for enhanced dc magnetic field sensitivity. *Phys. Rev. B* **2011**, *84*, 195204.

- (31) Booth, K.; Gray, I.; Dan Dahlberg, E. Determining the AC susceptibility of thin metal films using the anisotropic magnetoresistance. *Journal of Magnetism and Magnetic Materials* **2021**, *523*, 167631.
- (32) Schoenfeld, R. S.; Harneit, W. Real Time Magnetic Field Sensing and Imaging Using a Single Spin in Diamond. *Phys. Rev. Lett.* **2011**, *106*, 030802.
- (33) Zhang, T.; Pramanik, G.; Zhang, K.; Gulka, M.; Wang, L.; Jing, J.; Xu, F.; Li, Z.; Wei, Q.; Cigler, P.; Chu, Z. Toward Quantitative Bio-sensing with Nitrogen–Vacancy Center in Diamond. *ACS Sensors* **2021**, *6*, 2077–2107.
- (34) Hatano, Y.; Sekiguchi, T.; Iwasaki, T.; Hatano, M.; Harada, Y. Magnetic Field Imaging of Superparamagnetic Particles Using High-Density, Perfectly Oriented NV Centers in Diamond CVD Film. *physica status solidi (a)* **2018**, *215*, 1800254.
- (35) Sandler, S. E.; Fellows, B.; Mefford, O. T. Best Practices for Characterization of Magnetic Nanoparticles for Biomedical Applications. *Analytical Chemistry* **2019**, *91*, 14159–14169.

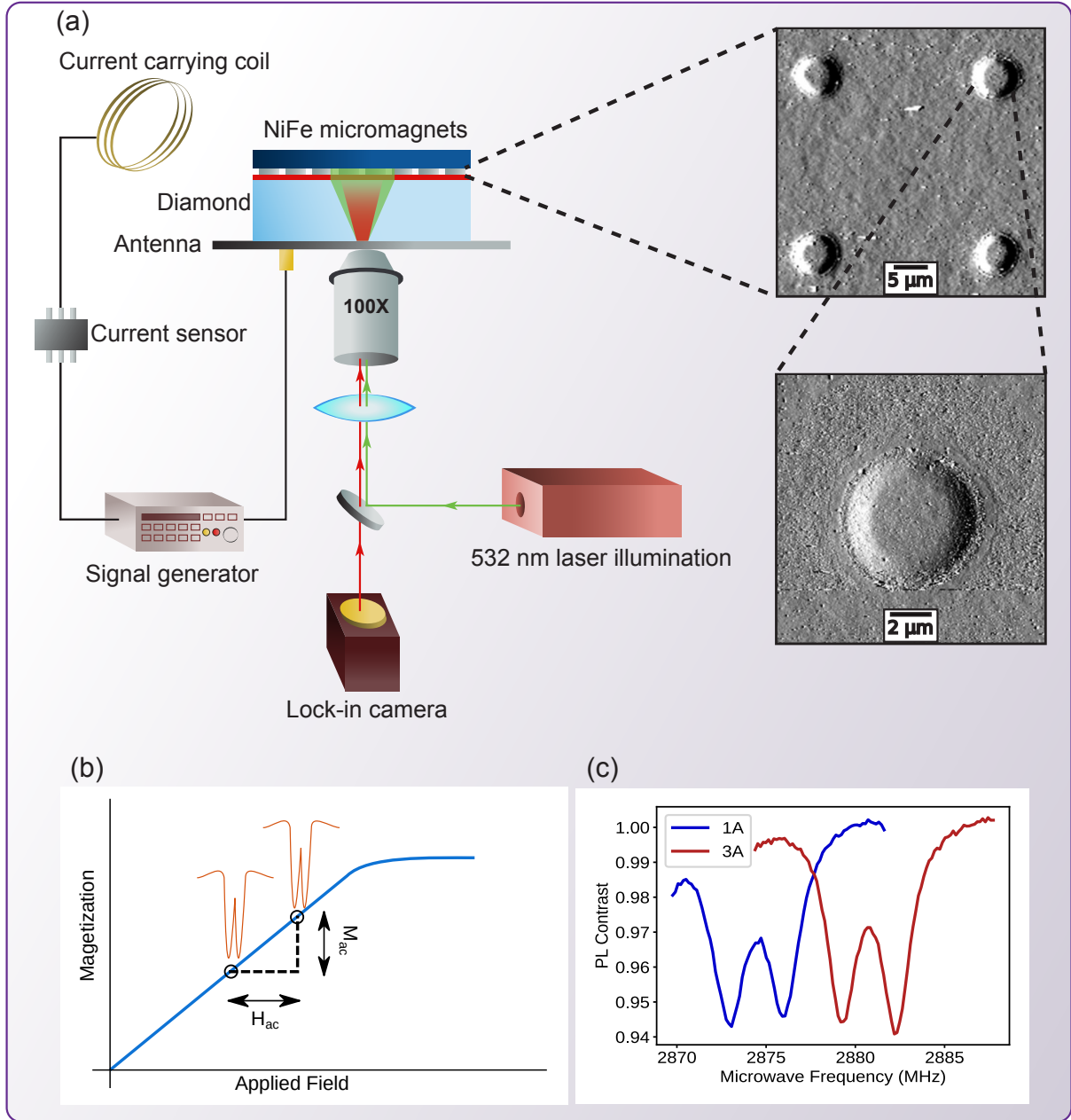


Figure 1: (a). A schematic representation of the fabricated Py micro-magnet array placed on top of a 1 μm thin NV⁻ layer in a diamond for wide-field magnetic imaging. A current sensor is used to dynamically set the microwave frequency based on the current passing through the current carrying coil. The inset shows the AFM image of the fabricated Py micro-magnets. (b). The stray field from the micro-magnets is measured from ODMR signal at various points on the MH curve. The dipole moment can be extracted from the stray field. (c). ODMR signal from a single pixel at two different excitation currents.

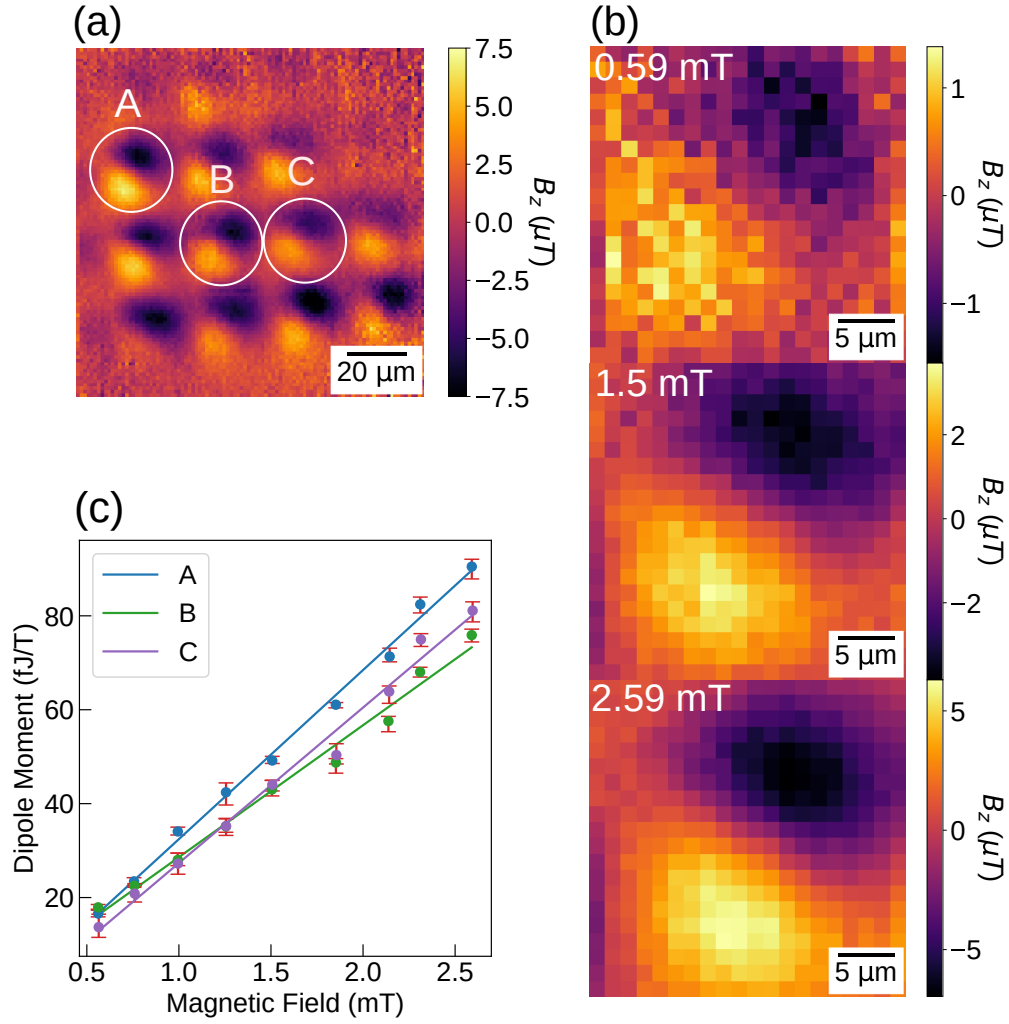


Figure 2: (a). Stray magnetic field along z -axis from an array of NiFe micro-magnets at an applied field of 2.59 mT. Three micro-magnets A , B , and C have been shown for reference. (b). Stray magnetic field from micro-magnet A at applied fields of 0.56 mT, 1.5 mT, and 2.59 mT. (c). Dipole moment of micro-magnets A , B , C plotted against applied magnetic field. Linear functions $m_A = -3.55 + 36b$, $m_B = 0.5 + 28.1b$, $m_C = -5.76 + 33.11b$ are used to fit the dipole moment of micro-magnets A , B , and C versus applied magnetic field. Units of m_A , m_B , m_C , and b are same as shown in the plot.

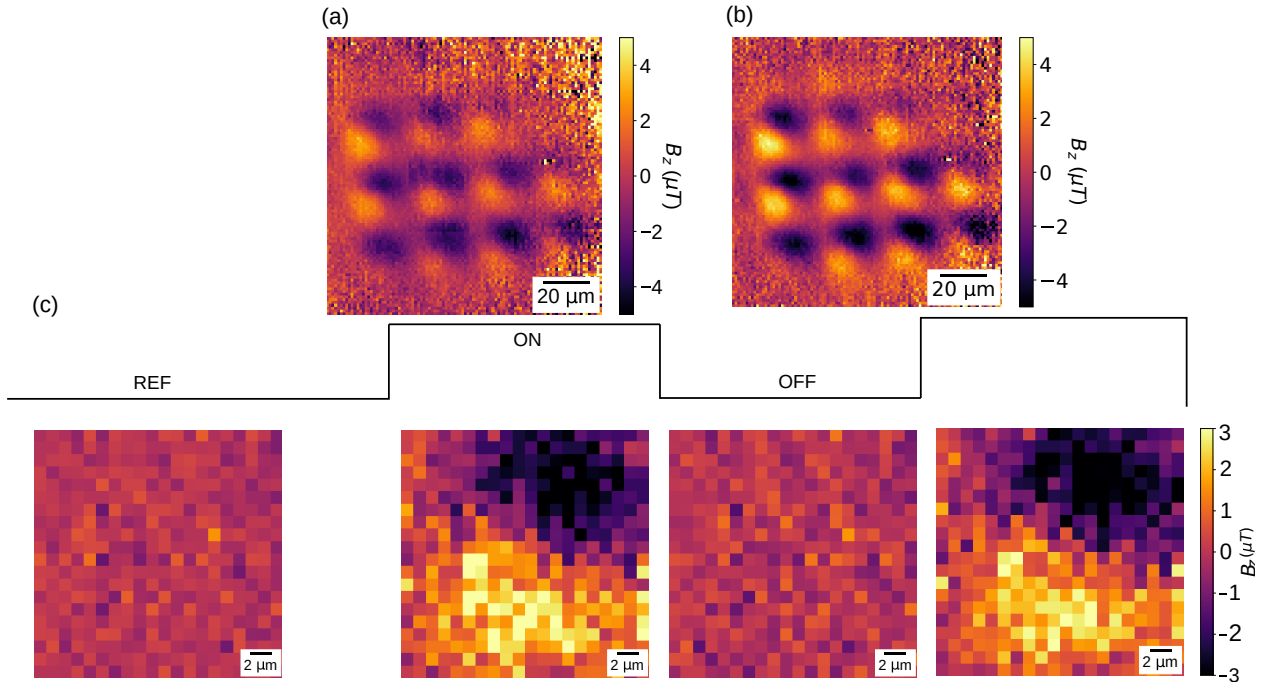


Figure 3: (a). Stray DC magnetic field maps obtained by fitting the full ODMR spectrum at applied fields of 0.75 mT, and 1.85 mT. (b). Change in stray field from micro-magnet A when the magnetic field is varied between 0.75 mT, and 1.85 mT. Frame REF is obtained by a 0.75 mT for elongated time and acts as reference. Subsequently, frames acquired when the excitation field is high are collectively labeled ON frames and those with low excitation field are collectively named OFF frames.

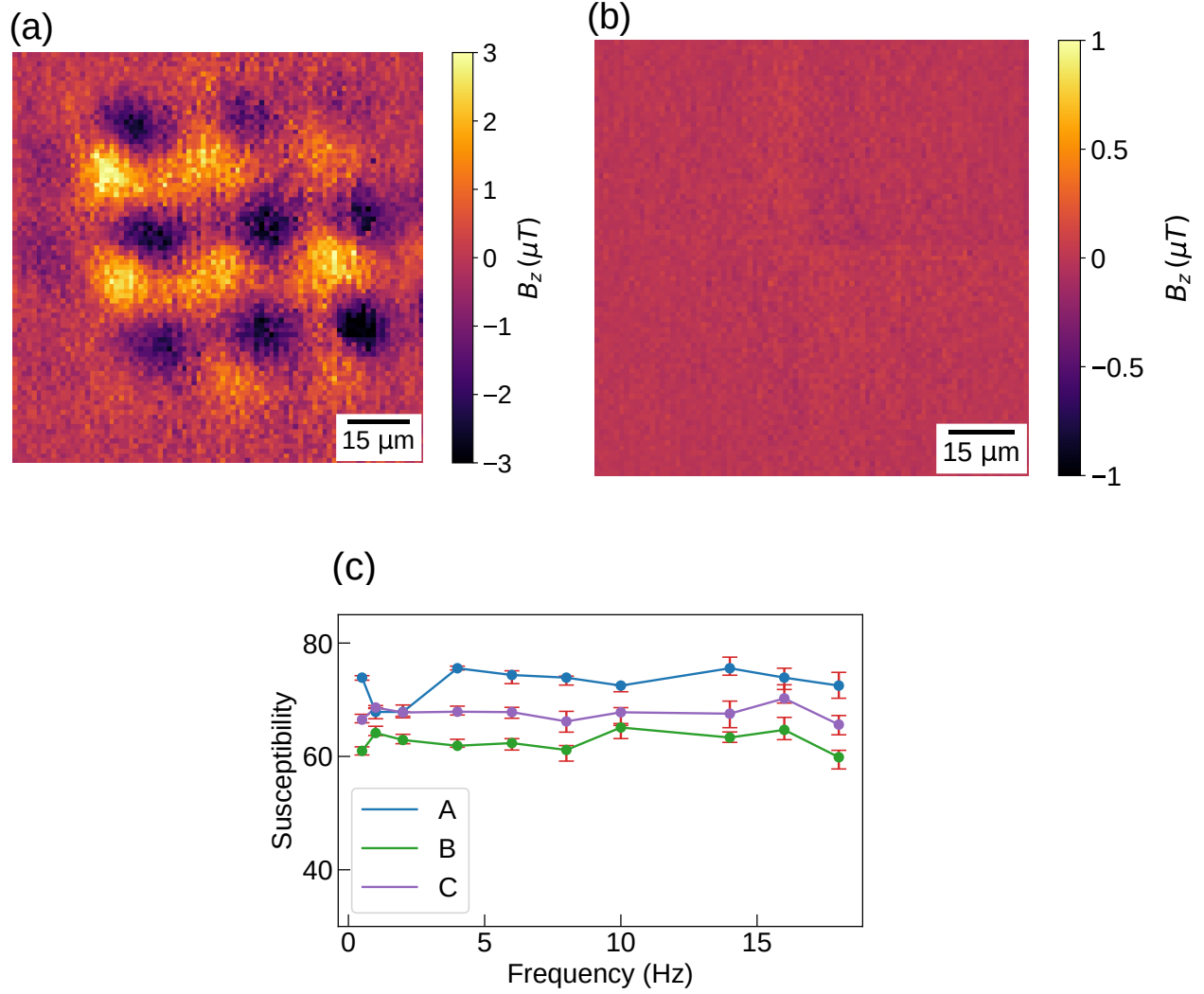


Figure 4: (a). In-phase and out-of-phase stray magnetic field from the micro-magnet array at a frequency of 18 Hz obtained by subtracting frames ON and OFF and OFF and REF respectively as shown in Fig. 3.(b). Real part of susceptibility (χ') of micro-magnet A , B , and C plotted against frequency applied excitation frequency.